Title

Large magnetoelectric resistance in the topological Dirac semimetal α-Sn

Journal

Science Advances, 8(30)

ISSN

2375-2548

Authors

Zhang, Yuejie

Kalappattil, Vijaysankar

Liu, Chuanpu

et al.

Publication Date

2022-07-29

DOI

10.1126/sciadv.abo0052

Peer reviewed

PHYSICS

Large magnetoelectric resistance in the topological Dirac semimetal α-Sn

Yuejie Zhang[1,2]†, Vijaysankar Kalappattil[1]†, Chuanpu Liu[1]†, M. Mehraeen[3], Steven S.-L. Zhang[3]†, Jinjun Ding[1], Uppalaiah Erugu[4], Zhijie Chen[5], Jifa Tian[4], Kai Liu[5], Jinke Tang[4], Mingzhong Wu[1]*

The spin-momentum locking of surface states in topological materials can produce a resistance that scales linearly with magnetic and electric fields. Such a bilinear magnetoelectric resistance (BMER) effect offers a new approach for information reading and field sensing applications, but the effects demonstrated so far are too weak or for low temperatures. This article reports the first observation of BMER effects in topological Dirac semimetals; the BMER responses were measured at room temperature and were substantially stronger than those reported previously. The experiments used topological Dirac semimetal α-Sn thin films grown on silicon substrates. The films showed BMER responses that are 10^6 times larger than previously measured at room temperature and are also larger than those previously obtained at low temperatures. These results represent a major advance toward realistic BMER applications. Significantly, the data also yield the first characterization of three-dimensional Fermi-level spin texture of topological surface states in α-Sn.

INTRODUCTION

Surface electronic states in topological materials exhibit spin-momentum locking. That is, the spin direction of the relevant conduction electrons is locked to the momentum at right angles. In applicable two-dimensional (2D) momentum space, this locking manifests itself as a chiral Fermi contour upon which the spins point along the tangential direction everywhere, as sketched in Fig. 1A. Such a Fermi contour usually takes a circular shape. It, however, can morph into a hexagonally warped contour, as in Fig. 1B, if the material structure has threefold rotational symmetry (*1*–*7*). As one walks along such a hexagonal contour, the spins still rotate in a chiral manner as on the circular contour but now have an out-of-plane component. Such hexagonal warping exists in thin films of topological materials with (111)-oriented cubic structures or *c* axis–oriented rhombohedral structures.

The spin-momentum locking gives rise to two important effects: prohibition of electron backscattering and efficient conversion between charge and spin currents. The first effect opens the possibility of dissipation-free information transport. The second allows one to use charge currents to control magnetic properties (*8*–*14*).

[1]Department of Physics, Colorado State University, Fort Collins, CO 80523, USA. [2]School of Optical and Electronic Information, Huazhong University of Science and Technology, Wuhan, Hubei 430074, China. [3]Department of Physics, Case Western Reserve University, Cleveland, OH 44106, USA. [4]Department of Physics and Astronomy, University of Wyoming, Laramie, WY 82071, USA. [5]Physics Department, Georgetown University, Washington, DC 20057, USA.
*Corresponding author. Email: mwu@colostate.edu
†These authors contributed equally to this work.

There is another newly reported spin-momentum locking effect: a bilinear magnetoelectric resistance (BMER) response (*15*–*18*). This effect occurs in topological materials with hexagonal warping contours as introduced above. The warping results in a resistance that scales linearly with magnetic and electric fields and varies with the direction of the electric current relative to the crystallographic axes of the material. Such responses were first observed in the topological insulator Bi_2Se_3, with a BMER coefficient of $\chi = 0.6\ nm^2A^{-1}\ Oe^{-1}$ (*15*). Here, χ is the normalized BMER per unit magnetic field and per unit current density. The effect was then also observed for 2D electron gas on surfaces of $SrTiO_3$ crystals but with a substantially larger coefficient, $\chi = 500\ nm^2A^{-1}\ Oe^{-1}$ (*17*). These observations were made at relatively low temperatures (60 K for Bi_2Se_3; 7 K for $SrTiO_3$). More recent work shows that room-temperature BMER is also possible (*18*). This later response was seen in the Weyl semimetal WTe_2 but was significantly weaker, with χ=0.001 $nm^2A^{-1}\ Oe^{-1}$ only.

Figure 1 (C to E) provides a schematic guide to the BMER effect (*16*). First, when an electric field E (black arrow) is applied, as in Fig. 1C, in addition to the first-order correction to the electron distribution that yields an ordinary charge current, there is a second-order correction to the distribution that results in equal numbers of electrons populated in the surface states with opposite spins and velocities. The net effect is a pure spin current J_s (red arrow) that scales with the square of the electric field, namely, E^2. Second, when a magnetic field H (blue arrow) is applied, as in Fig. 1D, the flux of electrons with opposite spins is no longer balanced. As a result, J_s is partially converted to a charge current J_c (green arrow) that adds to

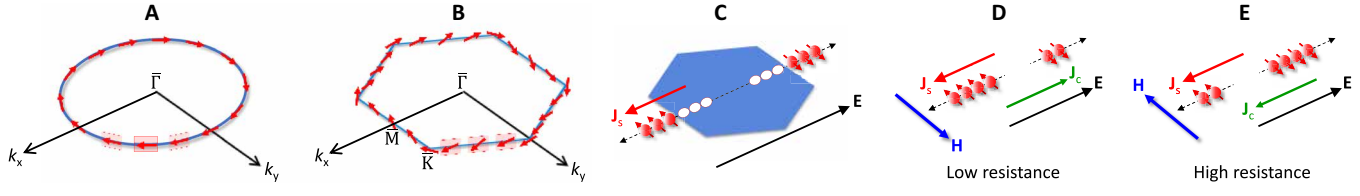

Fig. 1. BMER due to spin-momentum locking (*15 16*). (**A**) Spin texture on a circular Fermi contour of topological surface states (TSS). (**B**) Spin texture on a hexagonally warped Fermi contour. (**C**) Electric field E-induced generation of a pure spin current J_s. (**D**) Magnetic field H-induced partial conversion of J_s to a charge current J_c, giving rise to a lower resistance. (**E**) In comparison with (D), a flip in H leads to a flip in J_c and a higher resistance. The short red arrows denote spin directions.

the ordinary charge current and thereby gives rise to a lower resistance. Last, if H is reversed, as in Fig. 1E, J_c is also reversed and gives rise to a higher resistance.

This article reports a large room-temperature BMER response with a coefficient that is orders of magnitude larger than that in previous work. The experiments used a topological Dirac semimetal (TDS) α-Sn, in contrast to the topological insulators, 2D electron gas, and Weyl semimetals in previous work. (111)-oriented TDS α-Sn thin films in the 4- to 6-nm thickness range were grown on silicon substrates by sputtering at room temperature. Room-temperature measurements showed a resistance that scaled linearly with both the magnetic field and the charge current and strongly depended on the current direction relative to the crystalline axes of the films. The data showed χ values in the range of 2900 nm^2A^{-1} Oe^{-1}. This coefficient is 10^6 times larger than that obtained at room temperature for Weyl semimetals (*18*). It is also substantially larger than previous values obtained at low temperatures (*15*, *17*). Such a giant effect is most likely due to the low carrier density and spatial asymmetry of the α-Sn films.

Furthermore, the data also provide evidence for Fermi contour warping in TDS α-Sn films. The spins on the hexagonal contour (Fig. 1B) lie in-plane at the hexagon vertexes but tilt ±30° out-of-plane at the middle points of the hexagon sides.

Before bringing in the key data, it is useful to establish three important points. First, the BMER effect offers a totally new approach for information reading and field sensing technologies. While previous results were too weak or manifested only at low temperatures, the very large, room-temperature BMER reported here points to the possibility of real applications. This technological importance is further highlighted by the following: (i) The effects have been obtained in a single-material, single-element thin film; this can significantly simplify device fabrication. (ii) The α-Sn films were grown on silicon, a common industrial substrate, by sputtering, an industry-friendly technique. Second, this work shows the technological potential for surface states in TDS α-Sn. There have been major efforts to develop spintronic applications of surface states in topological insulators (*8*–*14*), but corresponding efforts for TDS systems up to now have been limited. Third, this work also represents the first-ever measurement of 3D Fermi contours in α-Sn. There have been extensive angle-resolved photoemission spectroscopy (ARPES) measurements on surface and bulk states in α-Sn (*19*–*26*), but none of them have even touched on the 3D aspect of the Fermi-level spin texture in α-Sn.

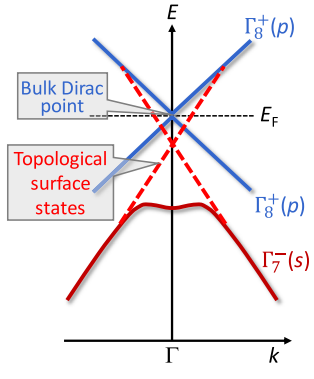

Fig. 2. Band structure in TDS α-Sn thin films (*22*, *27*).

α-Sn has a diamond cubic structure. Unstrained α-Sn is a gapless semiconductor in which the quadratic conduction and valence bands touch each other at the Γ point near the Fermi level. In the presence of a tensile strain along the [001] or [111] direction, however, the two bands cross each other near the Fermi level. This band crossing forms two Dirac points and gives rise to a TDS phase (*22*, *27*–*29*). One of these Dirac points is shown in Fig. 2. The topological nature of the TDS α-Sn originates from the band inversion: The bands (Γ_8^+) near the Fermi level are derived from *p* electrons, while the *s* electron–derived band (Γ_7^-) with opposite parity is below the Fermi level, as illustrated in Fig. 2. The topological surface states (TSS) bridge the Γ_8^+ conduction band and the Γ_7^- valence band (*22*, *27*). The Fermi level cut across the TSS cone corresponds to the circular contour in Fig. 1A.

In this work, (111)-oriented α-Sn thin films were grown on Si substrates by sputtering (*30*, *31*). The film growth details and structural properties are given in the Supplemental Materials. The lattice constant of α-Sn (6.489 Å) is larger than that of Si (5.431 Å). This mismatch yields a perpendicular tensile strain in the α-Sn films. This strain pushes the films into a TDS phase (*22*, *27*–*29*). The (111) orientation leads to the hexagonal warping depicted in Fig. 1B.

RESULTS

Figures 3 and 4 present the main results, namely, the BMER data obtained on 4-nm-thick α-Sn films. As in previous work (*15*, *17*, *18*), the experiments were based on Hall bar structures and measurements of the second-harmonic resistance in response to an AC current. The Hall bar drive current takes the form $I(t) = I_0 \cos(\omega t)$, where I_0 is the current amplitude, and ω is the frequency. The total longitudinal resistance is taken to be composed of an ordinary resistance R_0 and a BMER component $CI(t)$. Then, the longitudinal voltage in the α-Sn film can be evaluated as

$$\begin{aligned} V &= [I(t)][R_0 + CI(t)] = [I_0\cos(\omega t)][R_0 + CI_0\cos(\omega t)] \\ &= \frac{1}{2}CI_0^2 + R_0 I_0\cos(\omega t) + \frac{1}{2}CI_0^2\cos(2\omega t) \end{aligned} \quad (1)$$

Division of Eq. 1 by I_0 gives the longitudinal resistance as

$$\frac{V}{I_0} = \frac{1}{2}CI_0 + R_0\cos(\omega t) + \frac{1}{2}CI_0\cos(2\omega t) \quad (2)$$

One can see that the coefficient of cos(ω*t*) in Eq. 2 is the ordinary resistance, whereas that of cos(2ω*t*) is one-half the BMER. Second-harmonic signal measurements, therefore, allow for a direct measurement of the BMER response. In the discussions below, a new parameter, $R_{2\omega}$, is used to denote the second-harmonic resistance $\frac{1}{2}CI_0$.

Figure 3 gives the basic $R_{2\omega}$ data. Figure 3 (A to C) shows the $R_{2\omega}$ data obtained by rotating the field H in different planes. For clarity, the measurement configurations are shown in the upper diagrams in the panels. The red and black curves in Fig. 3 (A and B) are fits to sine and cosine functions, respectively. The red and black curves in Fig. 3C are the same as those in Fig. 3 (A and B). The blue curve corresponds to the sum of the red and black curves. Figure 3D shows $\Delta R_{2\omega}$, the amplitude of the sinusoidal $R_{2\omega}$, versus angle response, as a function of the current amplitude I_0 and the field strength *H*. The current or the Hall bar length is along the $[11\bar{2}]$ axis of the α-Sn film. The effects of the current direction are discussed shortly.

Four important results are evident from the data in Fig. 3. (i) The data in Fig. 3A indicate that $R_{2\omega}$ takes the maximum and the minimum for a magnetic field along $\hat{\mathbf{y}}$ and $-\hat{\mathbf{y}}$, respectively. This is consistent

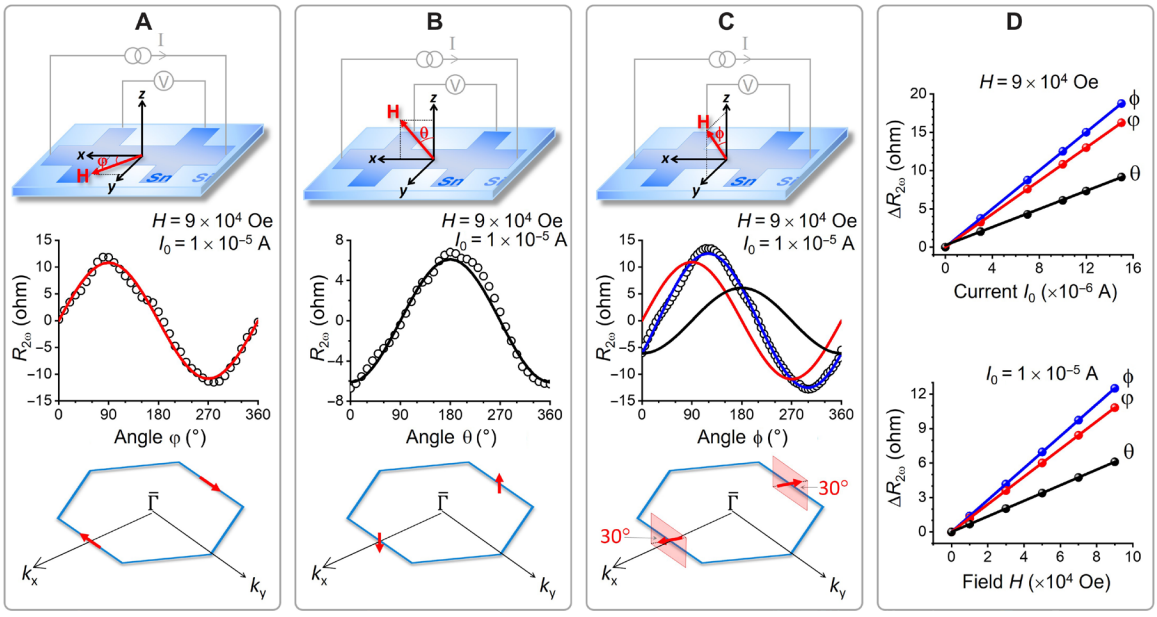

Fig. 3. Second-harmonic resistance ($R_{2\omega}$) as a function of the magnetic field angle for a 4-nm-thick α-Sn film. The circles show the data, the curves show sinusoidal fits, and the lines show linear fits. The field strength H and the current amplitude I_0 are indicated. In (**C**), the red curve shows the fit in (**A**), and the black curve shows the fit in (**B**); the blue curve is the sum of the red and black curves. In (**D**), $\Delta R_{2\omega}$ is the amplitude of the sinusoidal $R_{2\omega}$ versus angle response.

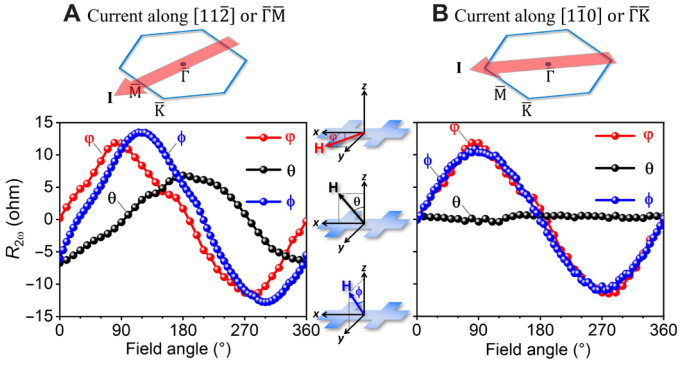

Fig. 4. Second-harmonic resistance ($R_{2\omega}$) as a function of the magnetic field angle for a 4-nm α-Sn film. The data in (**A**) were measured with a Hall bar whose length is along [11$\bar{2}$] of the α-Sn film, while those in (**B**) were measured with a Hall bar with its length along [1$\bar{1}$0].

with the picture depicted in Fig. 1 (D and E). It suggests that the projection of the spin vector on the *xy* plane points along the *y* axis, as in the bottom diagram in Fig. 3A. The response in Fig. 3A also represents a unidirectional magnetoresistance (UMR) along the *y* axis; the resistance is the largest for $\mathbf{H}\|\hat{\mathbf{y}}$ and is the smallest for $\mathbf{H}\|(-\hat{\mathbf{y}})$. (ii) The data in Fig. 3B show a UMR along the *z* axis. This confirms that the spin has a nonzero out-of-plane component, as depicted in the bottom diagram in Fig. 3B. (iii) Considered together, the data in Fig. 3 (A and B) suggest that the spin vector lies in the *yz* plane. This is confirmed by the data in Fig. 3C. Furthermore, the data show a $R_{2\omega}$ maximum at a field angle of $\phi \approx 120°$ and a minimum at $\phi \approx 300°$. This indicates that the spin vector is tilted ~30° out of the *xy* plane, as in the bottom diagram in Fig. 3C. These results are strongly supported by the nice agreement between the experimental response and the blue curve in Fig. 3C. (iv) The data in Fig. 3D show that $\Delta R_{2\omega}$ scales linearly with both I_0 and H.

Figure 4 shows the $R_{2\omega}$ versus field angle responses for the currents applied along two different crystalline axes: [11$\bar{2}$] and [1$\bar{1}$0], which correspond to the $\bar{\Gamma}\bar{M}$ and $\bar{\Gamma}\bar{K}$ momentum space lines in Fig. 1B, respectively. The data in Fig. 4A are the same as in Fig. 3 (A to C). The relevant crystalline axes are defined in the Supplementary Materials. The data in Fig. 4A show that when the current is applied along $\bar{\Gamma}\bar{M}$, the spins are in the *yz* plane and tilt at an angle of about 30° away from the *y* axis, as discussed above. In contrast, if the current is along $\bar{\Gamma}\bar{K}$, then $R_{2\omega}$ exhibits a notable angle dependence for field rotation in the *xy* plane but shows almost no angle dependence for field rotation in the *xz* plane, as shown in Fig. 4B. These responses indicate that the spins point along the *y* axis and have a zero out-of-plane component. Such spin orientation is consistent with the spin texture depicted in Fig. 1B.

Together, the results above clearly demonstrate the presence of the BMER in the 4-nm α-Sn films. The same responses have been confirmed in multiple samples. As an example, Fig. 5 gives the data measured on an α-Sn film that is thicker. Figure 5A shows the $R_{2\omega}$ versus field angle responses for the Hall bar axis and current applied along [11$\bar{2}$], which correspond to $\bar{\Gamma}\bar{M}$ in momentum space. Figure 5B gives companion data measured for a current 60° away from [11$\bar{2}$], along $\bar{\Gamma}\bar{M}'$ in momentum space. The data show two key results. First, the field angle dependences in Fig. 5A are about the same as those presented above for the 4-nm film. This consistency supports the results discussed above. Second, when the current direction is rotated from $\bar{\Gamma}\bar{M}$ to $\bar{\Gamma}\bar{M}'$, the φ dependence remains the same, but the θ response flips in sign. This indicates that a rotation in the current direction does not affect the in-plane component of the spin vector but reverses the sign of the out-of-plane component. This is consistent with the chiral spin texture depicted in Fig. 1B. In addition, the data show that $\Delta R_{2\omega}$ is smaller than that for the 4-nm film. This result,

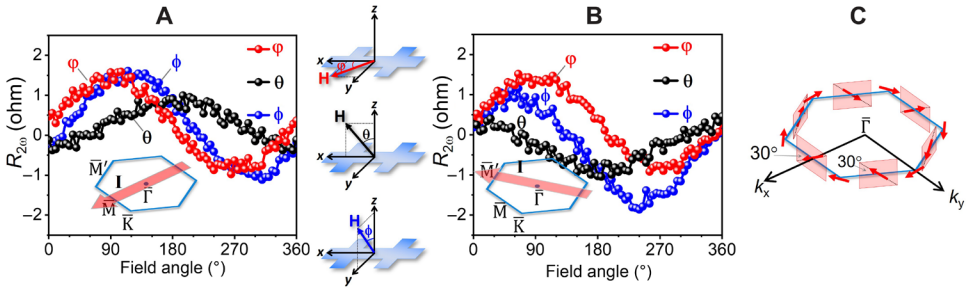

Fig. 5. BMER responses in a 5.8-nm α-Sn film. (**A**) $R_{2\omega}$ versus field angle responses measured with currents applied along $\overline{\Gamma M}$. (**B**) $R_{2\omega}$ versus field angle responses measured with currents applied along $\overline{\Gamma M}'$. (**C**) Spin texture on the Fermi contour.

together with the data in fig. S8, indicates that the BMER decreases with an increase in the film thickness. Possible reasons include that as the thickness increases, the phase of a Sn film transforms from pure α to a mixture of α and β and then to β dominant (*31*). This is discussed further in the Supplementary Materials. It is worthy to note that although the first-harmonic resistance is irrelevant to the BMER and is therefore not presented in Figs. 3 to 5, it yields important information about the carrier density and mobility of the bulk and surface states in the α-Sn films, as reported previously (*31*).

DISCUSSION

BMER coefficient

Previous studies have characterized the BMER effect in terms of a coefficient (*17*)

$$\chi = \frac{2\Delta R_{2\omega}}{R_0 J_0 H} \tag{3}$$

where $J_0 = \frac{I_0}{wt}$ (w, Hall bar width; t, film thickness) is the current density. With the data in Fig. 3, one obtains $\chi \approx 2900$ nm^{2}A^{-1} Oe^{-1}. This coefficient is 10^6 times larger than the value obtained previously at room temperature for the Weyl semimetal WTe_2 (*18*). It is also markedly larger than the values measured previously at low temperatures (*15*, *17*).

The large BMER in TDS α-Sn films possibly originates from the following facts. First, the 2D carrier density (n) of the TSS in α-Sn films is relatively low. One can show theoretically that, in the presence of sizable warping, the BMER coefficient χ exhibits a strong inverse dependence on the carrier density: $\chi \sim \frac{1}{n^{2.5}}$ for an in-plane magnetic field and $\chi \sim \frac{1}{n^{3.5}}$ for an out-of-plane magnetic field (see section S5). A $\chi \propto \frac{1}{n^3}$ response has been reported for $SrTiO_3$ (*17*). Previous experiments have shown $n \approx 1.8 \times 10^{12}$ cm^{-2} for TSS in TDS α-Sn films (*31*), 3.0×10^{13} cm^{-2} for TSS in Bi_2Se_3 films (*32*), and 5.3×10^{13} to 7.7×10^{14} cm^{-2} for 2D electron gas in $SrTiO_3$ (*17*). One can see that n in TDS α-Sn films is more than one order of magnitude smaller than in either Bi_2Se_3 or $SrTiO_3$.

Second, the α-Sn film in this work does not have spatial inversion symmetry. Specifically, the film bottom surface at the interface with the Si substrate is smooth, while the top surface is relatively rough. For this reason, the electrons on the top surface may undergo more frequent scattering from nonmagnetic disorders than those on the bottom surface. The net effect is that the measured BMER can be attributed mainly to the spin-momentum locking at the bottom surface. If the film has inversion symmetry, the BMER responses from the two surfaces would cancel each other and thereby give rise to very weak overall responses, if not zero. This partially explains why χ in Bi_2Se_3 is only 0.6 nm^{2}A^{-1} Oe^{-1} (*15*). Note that among these two facts, the first one may play a more dominant role than the second, as discussed in section S5.

Spin texture of TSS

Together, the data in Figs. 4 and 5 show the 3D aspect of the spins of the Fermi-level TSS in TDS α-Sn. Specifically, the spin in the middle point of a side of the hexagonal Fermi contour is not exactly along the hexagon side but tilts 30° out-of-plane. As one goes along the hexagonal contour to a vertex, the spin rotates into the plane. As one goes further to the middle point of the next hexagon side, the spin tilts −30° out-of-plane. This spin rotation is illustrated in Fig. 5D. There have been considerable ARPES works on the band structure of α-Sn (*19*–*26*), including spin-resolved ARPES measurements (*19*, *20*). However, none of those studies have touched on the 3D features of the spins on the Fermi contours of the TSS reported here.

The out-of-plane component (s_z) of the spin depends on the properties of the TSS at the Fermi level. These properties include the Fermi velocity (v_F), the Fermi wave number (k_F), and the strength of the hexagonal warping (λ). If one denotes $\varnothing_k$ as the angle between the $\overline{\Gamma M}$ direction and the wave vector (the current direction), s_z can be evaluated as (*1*, *15*)

$$s_z = \frac{\cos(3\varnothing_k)}{\sqrt{[\cos(3\varnothing_k)]^2 + \left(\frac{\hbar v_F}{\lambda k_F^2}\right)^2}} \tag{4}$$

where $\hbar$ is the reduced Planck constant. The $\cos(3\varnothing_k)$ term dictates the dependence of the BMER on the current direction as presented in Figs. 4 and 5, as well as the threefold symmetry of the chiral spin texture illustrated in Fig. 5D. For the data in Figs. 4A and 5A, one has $\varnothing_k = 0$ and $s_z = \sin 30°$. Taken these parameters and $v_F = \frac{4}{\hbar} \times 10^{-10}$ eV · m and $k_F = 3.39 \times 10^8$ m^{-1} from previous experiments (*22*, *31*), one can use Eq. 4 to estimate the warping parameter as $\lambda \approx 2$ eV · nm^3. This value is about one order of magnitude larger than the values reported for Bi_2Se_3 (*4*, *6*, *7*, *15*).

Final remarks

Five final remarks are as follows.

1) As discussed above, the BMER depends on the properties of the TSS at the Fermi level. As a result, further work is of great interest that explores the effects of the Fermi level on the BMER, with an aim to maximize the effect in the TDS α-Sn. Possible strategies to tune the Fermi level include doping (*19*), capping (*24*), and voltage gating.

2) Although this work reports the first measurements of the spin canting angle and warping parameter for the hexagonal Fermi contour of the TSS in TDS α-Sn, the measurements were somewhat indirect. It will be of great interest to directly map the 3D spin texture in the future. One note about the spin canting: In the TSS, the momentum is locked to real spin, and the spin canting arises from the cubic spin-orbit coupling at the surface. Because of the C_3 rotation symmetry along the film normal and the time-reversal symmetry, the spin-orbit coupling takes the form $(k_+^3 + k_-^3)\sigma_z$, where $k_\pm = k_x \pm ik_y$, and σ_z denotes the z component of the spin. The term leads to a warped Fermi contour and spin tilting along certain **k** directions (*3*).

3) The hexagonal warping contour in this work is a consequence of the threefold symmetry of the (111) α-Sn films, as mentioned above. In topological insulator α-Sn films that are (001) oriented and therefore do not have threefold symmetry, there are also magnetoresistances that scale linearly with magnetic and electric fields, as mentioned in (*33*). However, these magnetoresistances have nothing to do with the hexagonal warping but are associated with electron scattering by spin-orbit structural defects (*33*).

4) The BMER in this work is unidirectional in nature. However, it is different from the UMR found in bilayered structures consisting of a magnetic thin film and a heavy metal or topological insulator thin film (*34*–*40*). The latter has a different origin.

5) Recent work has demonstrated magnetoresistances in the semiconductor Ge and the topological insulator HgTe that scale linearly with both magnetic and electric fields but are independent of the current direction relative to the crystalline axes (*41*, *42*).The effect in Ge results from the interaction of the external magnetic field and a pseudomagnetic field associated with spin-split subsurface states (*41*), while that in HgTe originates from inhomogeneity-related scattering (*33*, *42*).

MATERIALS AND METHODS

Film growth

The Sn thin films are grown on single-crystal (111)-oriented Si substrates by DC magnetron sputtering. The substrates are rinsed sequentially with acetone and isopropyl alcohol before being loaded into the sputtering chamber. Before sputtering, the chamber has a base pressure of 2.0×10^{-8} torr; substrate biasing is performed that includes several cycles of Ar^+ ion sputtering of the substrate surface and the post-annealing of the substrate at 250°C. After the substrate biasing, the Sn deposition is then carried out at a substrate temperature of 7°C and at a growth rate of about 3 nm/min. The sputtering power is set to a moderate value of 10 W, to minimize the heating effect during the deposition. The major substrate biasing and sputtering control parameters are given in the Supplementary Materials.

Structural characterization

The surface morphology of the α-Sn thin films was characterized by atomic force microscopy. The crystalline properties of the α-Sn thin films were determined through x-ray diffraction (XRD) θ-2θ scan, XRD rocking curve, and XRD phi scan measurements. The detailed data are presented in the Supplementary Materials.

Device fabrication and measurements

To measure the electric transport properties of a Sn thin film, a Hall bar device is fabricated through photolithography and argon ion milling processes. To avoid heating the Sn film, a Hall bar pattern is first created on a Si substrate using a Microtech laser writer (LW405C). Then, the exposed sample surface is cleaned using ion milling. This process helps to remove any photoresist residue or SiO_2 on the device surface. Subsequently, deposition of a Sn thin film is carried out at a substrate temperature of 7°C via sputtering. Details about the device fabrication process, the dimensions of the Hall bar structure, and the electric transport measurements are presented in the Supplementary Materials.

SUPPLEMENTARY MATERIALS

Supplementary material for this article is available at https://science.org/doi/10.1126/sciadv.abo0052

REFERENCES AND NOTES

1. Y. L. Chen, J. G. Analytis, J.-H. Chu, Z. K. Liu, S.-K. Mo, X. L. Qi, H. J. Zhang, D. H. Lu, X. Dai, Z. Fang, S. C. Zhang, I. R. Fisher, Z. Hussain, Z.-X. Shen, Experimental realization of a three-dimensional topological insulator, Bi_2Te_3. *Science* **325**, 178–181 (2009).
2. D. Hsieh, Y. Xia, D. Qian, L. Wray, J. Dil, F. Meier, J. Osterwalder, L. Patthey, J. Checkelsky, N. Ong, A. V. Fedorov, H. Lin, A. Bansil, D. Grauer, Y. S. Hor, R. J. Cava, M. Z. Hasan, A tunable topological insulator in the spin helical Dirac transport regime. *Nature (London)* **460**, 1101–1105 (2009).
3. L. Fu, Hexagonal warping effects in the surface states of the topological insulator Bi_2Te_3. *Phys. Rev. Lett.* **103**, 266801 (2009).
4. K. Kuroda, M. Arita, K. Miyamoto, M. Ye, J. Jiang, A. Kimura, E. E. Krasovskii, E. V. Chulkov, H. Iwasawa, T. Okuda, K. Shimada, Y. Ueda, H. Namatame, M. Taniguchi, Hexagonally deformed Fermi surface of the 3D topological insulator Bi_2Se_3. *Phys. Rev. Lett.* **105**, 076802 (2010).
5. Z. Alpichshev, J. G. Analytis, J. H. Chu, I. R. Fisher, Y. L. Chen, Z. X. Shen, A. Fang, A. Kapitulnik, STM imaging of electronic waves on the surface of Bi_2Te_3: Topologically protected surface states and hexagonal warping effects. *Phys. Rev. Lett.* **104**, 016401 (2010).
6. Y. H. Wang, D. Hsieh, D. Pilon, L. Fu, D. R. Gardner, Y. S. Lee, N. Gedik, Observation of a warped helical spin texture in Bi_2Se_3 from circular dichroism angle-resolved photoemission spectroscopy. *Phys. Rev. Lett.* **107**, 207602 (2011).
7. M. Nomura, S. Souma, A. Takayama, T. Sato, T. Takahashi, K. Eto, K. Segawa, Y. Ando, Relationship between Fermi surface warping and out-of-plane spin polarization in topological insulators: A view from spin- and angle-resolved photoemission. *Phys. Rev. B* **89**, 045134 (2014).
8. Y. Fan, P. Upadhyaya, X. Kou, M. Lang, S. Takei, Z. Wang, J. Tang, L. He, L.-T. Chang, M. Montazeri, G. Yu, W. Jiang, T. Nie, R. N. Schwartz, Y. Tserkovnyak, K. L. Wang, Magnetization switching through giant spin–Orbit torque in a magnetically doped topological insulator heterostructure. *Nat. Mater.* **13**, 699–704 (2014).
9. J. Han, A. Richardella, S. A. Siddiqui, J. Finley, N. Samarth, L. Liu, Room-temperature Spin-orbit torque switching induced by a topological insulator. *Phys. Rev. Lett.* **119**, 077702 (2017).
10. Y. Wang, D. Zhu, Y. Wu, Y. Yang, J. Yu, R. Ramaswamy, R. Mishra, S. Shi, M. Elyasi, K.-L. Teo, Y. Wu, H. Yang, Room temperature magnetization switching in topological insulator-ferromagnet heterostructures by spin-orbit torques. *Nat. Commun.* **8**, 1364 (2017).
11. K. Yasuda, A. Tsukazaki, R. Yoshimi, K. Kondou, K. S. Takahashi, Y. Otani, M. Kawasaki, Y. Tokura, Current-nonlinear Hall effect and spin-orbit torque magnetization switching in a magnetic topological insulator. *Phys. Rev. Lett.* **119**, 137204 (2017).
12. Y. Li, Q. L. Ma, S. X. Huang, C. L. Chien, Thin films of topological Kondo insulator candidate SmB_6: Strong spin-orbit torque without exclusive surface conduction. *Sci. Adv.* **4**, eaap8294 (2018).
13. M. Dc, R. Grassi, J.-Y. Chen, M. Jamali, D. Reifsnyder Hickey, D. Zhang, Z. Zhao, H. Li, P. Quarterman, Y. Lv, M. Li, A. Manchon, K. A. Mkhoyan, T. Low, J.-P. Wang, Room-temperature high spin–orbit torque due to quantum confinement in sputtered $Bi_xSe_{(1-x)}$ films. *Nat. Mater.* **17**, 800–807 (2018).
14. N. H. D. Khang, Y. Ueda, P. N. Hai, A conductive topological insulator with large spin Hall effect for ultralow power spin–Orbit torque switching. *Nat. Mater.* **17**, 808–813 (2018).
15. P. He, S. S. L. Zhang, D. Zhu, Y. Liu, Y. Wang, J. Yu, G. Vignale, H. Yang, Bilinear magnetoelectric resistance as a probe of three-dimensional spin texture in topological surface states. *Nat. Phys.* **14**, 495–499 (2018).
16. S. S.-L. Zhang, G. Vignale, Theory of bilinear magneto-electric resistance from topological-insulator surface states. *Proc. SPIE* **10732**, 1073215 (2018).
17. P. He, S. M. Walker, S. S.-L. Zhang, F. Y. Bruno, M. S. Bahramy, J. M. Lee, R. Ramaswamy, K. Cai, O. Heinonen, G. Vignale, F. Baumberger, H. Yang, Observation of out-of-plane spin

texture in a $SrTiO_3$(111) two-dimensional electron gas. *Phys. Rev. Lett.* **120**, 266802 (2018).
18. P. He, C.-H. Hsu, S. Shi, K. Cai, J. Wang, Q. Wang, G. Eda, H. Lin, V. M. Pereira, H. Yang, Nonlinear magnetotransport shaped by Fermi surface topology and convexity. *Nat. Commun.* **10**, 1290 (2019).
19. A. Barfuss, L. Dudy, M. R. Scholz, H. Roth, P. Höpfner, C. Blumenstein, G. Landolt, J. H. Dil, N. C. Plumb, M. Radovic, A. Bostwick, E. Rotenberg, A. Fleszar, G. Bihlmayer, D. Wortmann, G. Li, W. Hanke, R. Claessen, J. Schäfer, Elemental topological insulator with tunable Fermi level: Strained α-Sn on InSb(001). *Phys. Rev. Lett.* **111**, 157205 (2013).
20. Y. Ohtsubo, P. Le Fèvre, F. Bertran, A. Taleb-Ibrahimi, Dirac cone with helical spin polarization in ultrathin α-Sn(001) films. *Phys. Rev. Lett.* **111**, 216401 (2013).
21. J. C. Rojas-Sanchez, S. Oyarzun, Y. Fu, A. Marty, C. Vergnaud, S. Gambarelli, L. Vila, M. Jamet, Y. Ohtsubo, A. Taleb-Ibrahimi, P. LeFevre, F. Bertran, N. Reyren, J. M. George, A. Fert, Spin to charge conversion at room temperature by spin pumping into a new type of topological insulator: α -Sn films. *Phys. Rev. Lett.* **116**, 096602 (2016).
22. C.-Z. Xu, Y.-H. Chan, Y. Chen, P. Chen, X. Wang, C. Dejoie, M.-H. Wong, J. A. Hlevyack, H. Ryu, H.-Y. Kee, N. Tamura, M.-Y. Chou, Z. Hussain, S.-K. Mo, T.-C. Chiang, Elemental topological Dirac semimetal: α -Sn on InSb(111). *Phys. Rev. Lett.* **118**, 146402 (2017).
23. V. A. Rogalev, T. Rauch, M. R. Scholz, F. Reis, L. Dudy, A. Fleszar, M.-A. Husanu, V. N. Strocov, J. Henk, I. Mertig, J. Schäfer, R. Claessen, Double band inversion in α -Sn: Appearance of topological surface states and the role of orbital composition. *Phys. Rev. B* **95**, 161117(R) (2017).
24. Q. Barbedienne, J. Varignon, N. Reyren, A. Marty, C. Vergnaud, M. Jamet, C. Gomez-Carbonell, A. Lemaitre, P. Le Fèvre, F. Bertran, A. Taleb-Ibrahimi, H. Jaffrès, J.-M. George, A. Fert, Angular-resolved photoemission electron spectroscopy and transport studies of the elemental topological insulator α -Sn. *Phys. Rev. B* **98**, 195445 (2018).
25. V. A. Rogalev, F. Reis, F. Adler, M. Bauernfeind, J. Erhardt, A. Kowalewski, M. R. Scholz, L. Dudy, L. B. Duffy, T. Hesjedal, M. Hoesch, G. Bihlmayer, J. Schäfer, R. Claessen, Tailoring the topological surface state in ultrathin α -Sn(111) films. *Phys. Rev. B* **100**, 245144 (2019).
26. I. Madarevic, U. Thupakula, G. Lippertz, N. Claessens, P.-C. Lin, H. Bana, S. Gonzalez, G. D. Santo, L. Petaccia, M. N. Nair, L. M. C. Pereira, C. V. Haesendonck, M. J. Van Bael, Structural and electronic properties of the pure and stable elemental 3D topological Dirac semimetal α-Sn. *APL Mater.* **8**, 031114 (2020).
27. H. Huang, F. Liu, Tensile strained gray tin: Dirac semimetal for observing negative magnetoresistance with Shubnikov–de Haas oscillations. *Phys. Rev. B* **95**, 201101 (2017).
28. D. Zhang, H. Wang, J. Ruan, G. Yao, H. Zhang, Engineering topological phases in the Luttinger semimetal α -Sn. *Phys. Rev. B* **97**, 195139 (2018).
29. L. D. Anh, K. Takase, T. Chiba, Y. Kota, K. Takiguchi, M. Tanaka, Elemental topological Dirac semimetal α-Sn with high quantum mobility. *Adv. Mater.* **33**, 2104645 (2021).
30. J. Ding, C. Liu, Y. Zhang, V. Kalappattil, R. Yu, U. Erugu, J. Tang, H. Ding, H. Chen, M. Wu, Large damping enhancement in Dirac-semimetal–Ferromagnetic-metal layered structures caused by topological surface states. *Adv. Funct. Mater.* **31**, 2008411 (2021).
31. J. Ding, C. Liu, V. Kalappattil, Y. Zhang, O. Mosendz, U. Erugu, R. Yu, J. Tian, A. DeMann, S. B. Field, X. Yang, H. Ding, J. Tang, B. Terris, A. Fert, H. Chen, M. Wu, Switching of a magnet by spin-orbit torque from a topological Dirac semimetal. *Adv. Mater.* **33**, 2005909 (2021).
32. P. Li, J. Kally, S. S.-L. Zhang, T. Pillsbury, J. Ding, G. Csaba, J. Ding, J. S. Jiang, Y. Liu, R. Sinclair, C. Bi, A. DeMann, G. Rimal, W. Zhang, S. B. Field, J. Tang, W. Wang, O. G. Heinonen, V. Novosad, A. Hoffmann, N. Samarth, M. Wu, Magnetization switching using topological surface states. *Sci. Adv.* **5**, eaaw3415 (2019).
33. A. Dyrdał, J. Barnaś, A. Fert, Spin-momentum-locking inhomogeneities as a source of bilinear magnetoresistance in topological insulators. *Phys. Rev. Lett.* **124**, 046802 (2020).
34. K. Olejník, V. Novák, J. Wunderlich, T. Jungwirth, Electrical detection of magnetization reversal without auxiliary magnets. *Phys. Rev. B* **91**, 180402 (2015).
35. C. O. Avci, K. Garello, A. Ghosh, M. Gabureac, S. F. Alvarado, P. Gambardella, Unidirectional spin Hall magnetoresistance in ferromagnet/normal metal bilayers. *Nat. Phys.* **11**, 570–575 (2015).
36. C. O. Avci, K. Garello, J. Mendil, A. Ghosh, N. Blasakis, M. Gabureac, M. Trassin, M. Fiebig, P. Gambardella, Magnetoresistance of heavy and light metal/ferromagnet bilayers. *Appl. Phys. Lett.* **107**, 192405 (2015).
37. K. Yasuda, A. Tsukazaki, R. Yoshimi, K. S. Takahashi, M. Kawasaki, Y. Tokura, Large unidirectional magnetoresistance in a magnetic topological insulator. *Phys. Rev. Lett.* **122**, 159903 (2019).
38. S. S.-L. Zhang, G. Vignale, Theory of unidirectional magnetoresistance in magnetic heterostructures. *Proc. SPIE* **10357**, 1035707 (2017).
39. N. H. D. Khang, P. N. Hai, Giant unidirectional spin Hall magnetoresistance in topological insulator – ferromagnetic semiconductor heterostructures. *J. Appl. Phys.* **126**, 233903 (2019).
40. T.-Y. Chang, C.-L. Cheng, C.-C. Huang, C.-W. Peng, Y.-H. Huang, T.-Y. Chen, Y.-T. Liu, C.-F. Pai, Large unidirectional magnetoresistance in metallic heterostructures in the spin transfer torque regime. *Phys. Rev. B* **104**, 024432 (2021).
41. T. Guillet, C. Zucchetti, Q. Barbedienne, A. Marty, G. Isella, L. Cagnon, C. Vergnaud, H. Jaffrès, N. Reyren, J.-M. George, A. Fert, M. Jamet, Observation of large unidirectional Rashba magnetoresistance in Ge(111). *Phys. Rev. Lett.* **124**, 027201 (2020).
42. Y. Fu, J. Li, J. Papin, P. Noel, M. Cosset-Chéneau, C. Grezes, T. Guillet, C. Thomas, Y. M. Niquet, P. Ballet, T. Meunier, J. P. Attane, A. Fert, L. Vila, Bilinear magnetoresistance in HgTe topological insulator: Opposite signs at opposite interfaces demonstrated by gate control. *arXiv* 2111.15594v1 (2021).
43. Ł. Gladczuk, L. Gladczuk, P. Dluzewski, G. van der Laan, T. Hesjedal, Study of spin pumping through α-Sn thin films. *Phys. Status Solidi RRL* **15**, 2100137 (2021).
44. S. Kaku, K. L. Hiwatari, J. Yoshino, Scanning tunneling microscopy of strained α-Sn(001) surface grown on InSb (001) substrate. *Appl. Surf. Sci.* **571**, 151347 (2022).
45. D. Culcer, E. H. Hwang, T. D. Stanescu, S. D. Sarma, Two-dimensional surface charge transport in topological insulators. *Phys. Rev. B* **82**, 155457 (2010).

Acknowledgments: We thank C. Patton for valuable suggestions. **Funding:** This work was supported by the U.S. Department of Energy, Office of Science, Basic Energy Sciences (DE-SC0018994). The growth and characterization of α-Sn thin films and the fabrication of the Hall bar structures were also supported by the U.S. National Science Foundation (EFMA-1641989; ECCS-1915849). Work at CWRU was supported by the College of Arts and Sciences at CWRU. Work at UW was supported by the U.S. National Science Foundation (DMR-1710512) and the U.S. Department of Energy, Office of Science, Basic Energy Sciences (DE-SC0020074; DE-SC0021281). Work at GU was supported by the U.S. National Science Foundation (DMR-2005108). **Author contributions:** Y.Z., V.K., and C.L. grew the materials, fabricated the devices, and performed the measurements, with help from J.D. M.M. and S.S.-L.Z. provided theoretical support. Y.Z., V.K., C.L., M.M., S.S.-L.Z., and M.W. carried out data analyses and discussed with J.Ti. U.E. and J.Ta. contributed to XRD and XRR measurements and analyses. Z.C. and K.L. performed XRD phi scan measurements and analyses. M.W. supervised the project. V.K., C.L., M.M., S.S.-L.Z., and M.W. wrote the paper and the Supplementary Materials, with feedback from all other co-authors. **Competing interests:** The authors declare that they have no competing interests. **Data and materials availability:** All data needed to evaluate the conclusions in the paper are present in the paper and/or the Supplementary Materials.

Submitted 6 January 2022
Accepted 14 June 2022
Published 29 July 2022
10.1126/sciadv.abo0052